PHILOSOPHICAL TRANSACTIONS A

royalsocietypublishing.org/journal/rsta

Research

Cite this article: Thiébaut M, Filipot J-F, Maisondieu C, Damblans G, Duarte R, Droniou E, Guillou S. 2020 Assessing the turbulent kinetic energy budget in an energetic tidal flow from measurements of coupled ADCPs. *Phil. Trans. R. Soc. A* **378**: 20190496. http://dx.doi.org/10.1098/rsta.2019.0496

Accepted: 31 January 2020

One contribution of 14 to a theme issue 'New insights on tidal dynamics and tidal energy harvesting in the Alderney Race'.

Subject Areas:
oceanography

Keywords:
turbulence, Reynolds stresses, coupled ADCPs, Alderney Race

Author for correspondence:
Maxime Thiébaut
e-mail: maxime.thiebaut@ite-fem.org

THE ROYAL SOCIETY PUBLISHING

Assessing the turbulent kinetic energy budget in an energetic tidal flow from measurements of coupled ADCPs

Maxime Thiébaut[1], Jean-François Filipot[1], Christophe Maisondieu[2], Guillaume Damblans[1], Rui Duarte[1], Eloi Droniou[3] and Sylvain Guillou[4]

[1]France Énergies Marines, Technopôle Brest-Iroise, 525 Avenue Alexis de Rochon, 29280 Plouzané, France
[2]IFREMER, ZI Pointe du diable, 29280 Plouzané, France
[3]DynamOcean SARL, 57 rue de Metz, 56000 Vannes, France
[4]Normandie Univ, UNICAEN, LUSAC, EA4253, site universitaire de Cherbourg, rue Louis Aragon, BP 78, 50130, Cherbourg-Octeville France

MT, 0000-0001-9316-6437; J-FF, 0000-0003-0875-8791

Two coupled four-beam acoustic Doppler current profilers were used to provide simultaneous and independent measurements of the turbulent kinetic energy (TKE) dissipation rate ε and the TKE production rate $\mathcal{P}$ over a 36 h long period at a highly energetic tidal energy site in the Alderney Race. The eight-beam arrangement enabled the evaluation of the six components of the Reynolds stress tensor which allows for an improved estimation of the TKE production rate. Depth-time series of ε, $\mathcal{P}$ and the Reynolds stresses are provided. The comparison between ε and $\mathcal{P}$ was performed by calculating individual ratios of ε corresponding to $\mathcal{P}$. The depth-averaged ratio $\varepsilon/\mathcal{P}$ averaged over whole flood and ebb tide were found to be 2.2 and 2.8 respectively, indicating that TKE dissipation exceeds TKE production. It is shown that the term of diffusive transport of TKE is significant. As a result, non-local transport is important to the TKE budget and the common assumption of a local balance, i.e. a balance between production and dissipation, is not valid at the measurement site.

This article is part of the theme issue 'New insights on tidal dynamics and tidal energy harvesting in the Alderney Race'.

1. Introduction

Turbulent processes are crucial in controlling the flow dynamics and the vertical exchange of momentum and scalars (temperature, salinity) throughout the water column. Over the three last decades, shelf sea circulation models such as TELEMAC, MARS or ROMS have been developed in order to simulate flows in various coastal areas from the regional scale down to the inshore scale (e.g. [1–7]). It is widely acknowledged that the parametrization of turbulence often represents a crucial weakness in the tidal flow generation of these numerical models. For computational efficiency, the models do not resolve turbulent fluctuations but parametrize their effect through turbulence closure schemes where quantity such as momentum is split into a mean and a fluctuating part. Testing the turbulence closure schemes with reliable field measurements is critical in order to better understand turbulent processes and thus improve the ability of numerical models to reconstruct the flow dynamics.

Information on the transport of momentum by turbulence is contained within the Reynolds stresses. Their knowledge, along with mean velocity profiles, is of prime importance since Reynolds stresses allow for the eddy viscosity, the most common parametrization of vertical mixing due to turbulence, to be computed. Reynolds stresses combined with measurements of velocity shear allow for the evaluation of another turbulence metric: the turbulent kinetic energy (TKE) production rate $\mathcal{P}$. Evaluation of the latter, together with the TKE dissipation rate ε, is useful to examine the TKE budget in order to understand the dynamics of the turbulence.

Reynolds stresses, as well as the TKE dissipation and production rates, vary both in space and time (e.g. [8–12]). This variability is usually estimated from velocity time series recorded by means of acoustic Doppler current profiler (ADCP), acoustic Doppler velocimeter (ADV) or vertical microstucture profiler (VMP). The last one is specifically used for the estimation of the TKE dissipation rate. Such instruments have been extensively used over the last 40 years (e.g. [11,13]). VMP employs shear probes to directly measure small-scale turbulence in lengthscales ranging from the millimetre to the metre. A VMP can be deployed sequentially at multiple locations within a study area of several square kilometres allowing for the assessment of the spatial distribution of the TKE dissipation rate. This is the main advantage of a VMP over ADCP and ADV. However, VMP measurements are limited in temporal resolution; thus, they do not allow capturing the spatial variation of the TKE dissipation rate throughout a tidal cycle.

ADVs are usually the preferred choice for turbulence measurements (e.g. [14–18]). In particular, they are used for turbulence characterization at small lengthscales. They are more accurate than ADCPs and VMPs as velocity recording is performed at higher sampling rate (up to 64 Hz) by converging beams at a fixed depth. However, ADVs only measure at one single point, and their deployment at a specifically chosen height requires complicated moorings and subsequent motion corrections to the raw data [19]. In addition, local measurement does not allow the identification of turbulence at all scales and deployment of multiple ADVs could affect the flow and is in any case relatively complicated.

ADCPs appear as a more practical alternative to ADVs and VMPs. ADCPs, using four diverging beams, are commonly used for the measurement of turbulent velocity fluctuations (e.g. [10,11,15,18,20]). They provide estimates of flow variability at different depth levels, often sampling the whole water column, and in the large frequency band covering timescales from one second to sub-tidal period. In addition, they can be deployed for long intervals of time (several months), allowing for an assessment of the flow variability over a wide range of timescales. However, due to relatively high noise level and diverging beams, reliable estimates of turbulence metrics can be done at a distance not exceeding several metres from the transducers.

The most commonly used method to estimate Reynolds stresses with ADCPs is the so-called variance method. With this technique, Reynolds stress profiles are estimated from along-beam velocity measurements, using the difference between the velocity variances along opposing beams, often with an explicit removal of the variance contributed by the Doppler noise. This method has been successfully used in a large number of shelf and estuarine studies of the evolution of the structure of turbulence (e.g. [8–10,21–25]). However, because of the spread

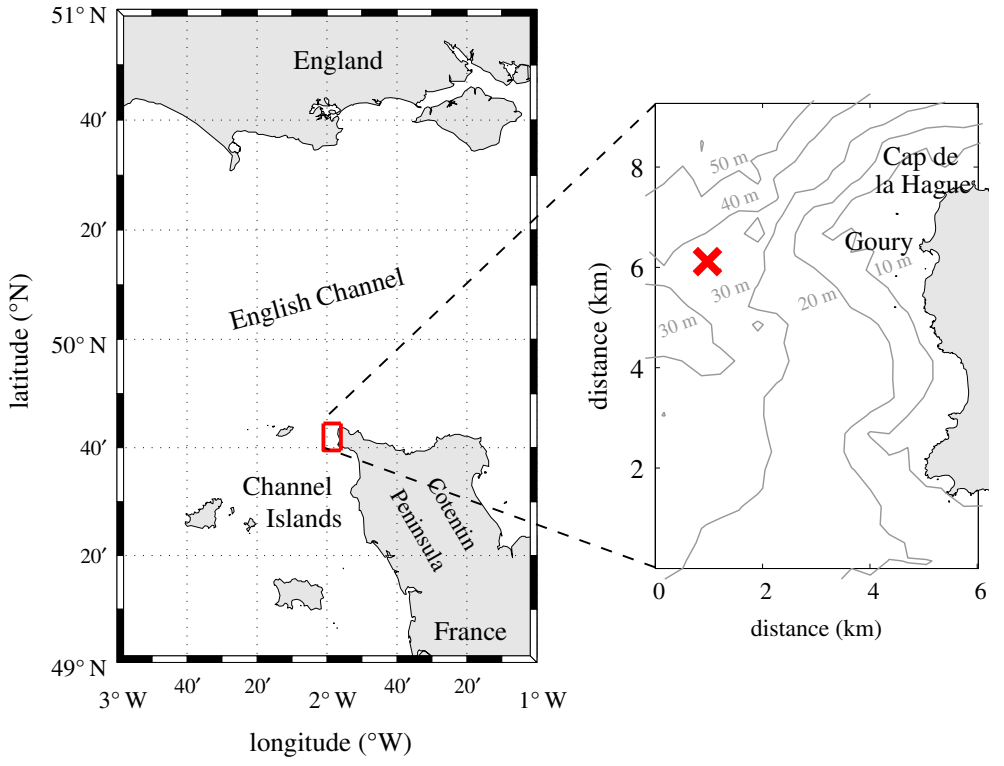

Figure 1. Left-hand side panel: map of the central part of the English Channel. Right-hand side panel: the eastern part of the Alderney Race with bathymetry (m) given in grey. Red cross denotes the location of the master and slave bottom-mounted ADCPs deployment site. (Online version in colour.)

between the beams of the ADCP, instantaneous estimates of velocity components from different beams cannot be combined directly. The spatial spreading can span several times the scale of the turbulent structures. Thus, the estimation of turbulence metrics requires that the second order moments of fluctuating velocities to be horizontally homogeneous so that the statistics of the turbulence are the same for each of the four beams [8]. Such assumption is required when using a single four-beam ADCP since it provides only two components (out of six) of the Reynolds stress tensor.

Vermeulen *et al.* [26] proposed a new methodology allowing for the full estimation of the Reynolds stress tensor. In their study, the authors employed two four-beam ADCPs operating in master–slave configuration. With the beam combination of the two coupled sensors, eight beams are available allowing one to resolve the six components of the Reynolds stress tensor. The coupled ADCPs set-up eliminates the potential bias in Reynolds stress estimates due to an inclination of the instrument. Recently, this method has been implemented to coupled ADCPs measurements performed within the Goulet de Brest, France [27]. In their study, Pieterse *et al.* [27] tested the effectiveness of a coupled ADCPs system mounted on a specific frame. The promising results encouraged us to go further in the exploitation of the coupled ADCPs methodology by deploying the system at a highly energetic site in the Alderney Race.

Measurements collected by the master ADCP (the slave ADCP was not considered) have been used by Thiébaut *et al.* [20] to provide the first estimation of ambient turbulence in the Alderney Race. The authors focused on assessing the turbulence lengthscales and timescales at mid-depth. The TKE dissipation rate ε and the integral lengthscale L were quantified using two independent methods: the spectral method and the structure function method. The spectral method was found to be more robust since it has provided ε and L estimates with standard deviations twice lower than that obtained from the structure function method.

The present study is an extension of the previous work of Thiébaut *et al.* [20]. The coupled ADCPs (eight-beam) arrangement is fully exploited since both the master and slave ADCPs are used to provide depth-time series of the six components of the Reynolds stress. Moreover, particular attention was paid to the TKE dissipation and production rate at different depths.

2. Data analysis and methods

(a) Experimental settings

Two upward-looking RDI Workhorse 600 kHz four-beam ADCPs were deployed on the seafloor (31 m mean water depth) approximately 4 km offshore, west of the port of Goury, in the eastern part of the Alderney Race (figure 1). The instruments were mounted on a specifically designed frame having the following features: 3.3 m long, 2.5 m wide and 2 100 kg weight (figure 2). The ADCPs collected data over a 38-day period, from 27 September to 3 November 2017. The instruments were coupled in a master–slave set-up and were set to record alternately the along-beam velocities at the pinging rate of 2 Hz. This measurement scheme was chosen in order to avoid any interference between the beams of the two sensors. Velocities were recorded with 1.3 m vertical resolution (bin size), starting 2.2 m from the seafloor (the first bin). The average standard deviation of the attitude parameters (heading θ_h, pitch θ_p and roll θ_r) of the master ADCP were found to be lower than 0.3°, indicating that the frame remained stable throughout the deployment.

A Cartesian coordinates system ($\mathcal{O}$, $\boldsymbol{e_x}$, $\boldsymbol{e_y}$, $\boldsymbol{e_z}$) was defined relative to the master ADCP, with the origin $\mathcal{O}$ located at the centre of the four transducers (figure 2). The average heading of the master ADCP was such that the opposite beam 1 and 2 were oriented in the streamwise direction, defining the $\boldsymbol{e_x}$-axis, whereas beams 3 and 4 pointed in the spanwise direction, defining the $\boldsymbol{e_y}$-axis. The slave ADCP was rotated relative to the master and they were located 0.5 m apart horizontally, following the set-up proposed by Vermeulen *et al.* [26]. The slave ADCP was rotated 45 degrees around the $\boldsymbol{e_z}$-axis, and 20 degrees around the $\boldsymbol{e_x}$-axis, resulting in a tilted ADCP with one beam pointed vertically upward (figure 2). This orientation is the best compromise between reasonable errors in the Reynolds stress estimates and the surface reflection which generate unusable velocity measurements [26].

(b) Wave conditions

Wave parameters such as the significant height H_s and the peak period T_p were extracted from the master ADCP measurements using WavesMon RDI software. Sea states were globally moderate with a mean and maximum H_s of 1.2 m and 4.5 m respectively (figure 3). Peak period ranged from 3.7 s to 14.5 s with a mean value of 7.8 s. The most dominant waves propagate from the southwestern direction [20] (result not shown). The mean angle between the wave propagation direction and the direction of the dominant tidal current was found to be 50° during ebb tide and 220° during flood tide.

Wave orbital motions generate coherent structures that appear in the variance of the along-beam velocity time series. Moreover, in marine environment, wave and turbulence spectral signature often occupy the same frequency band making any attempt of wave–turbulence separation challenging. Over the past two decades, numerous methods for reducing wave impact on turbulence measurements have been proposed (e.g. [20,24,28–31]). Advantages and disadvantages of these methods will not be exposed here as this is out of the scope of this paper. An appropriate way to avoid any wave contamination in turbulence measurements is to focus the analysis on a non-wavy period, i.e. on a period where wave orbital motions are negligible. Such a period was identified between 1 November 2017—01.45 UTC and 2 November 2017—13.45 UTC (grey region in figure 3). During this 36 h long period the depth averaged flow speed reached 3.5 m s^{-1}. The mean H_s and T_p were found to be 0.6 m and 6 s respectively. For such peak period, the increased variance associated with the wave motion does not penetrate to depths greater than 10 m.

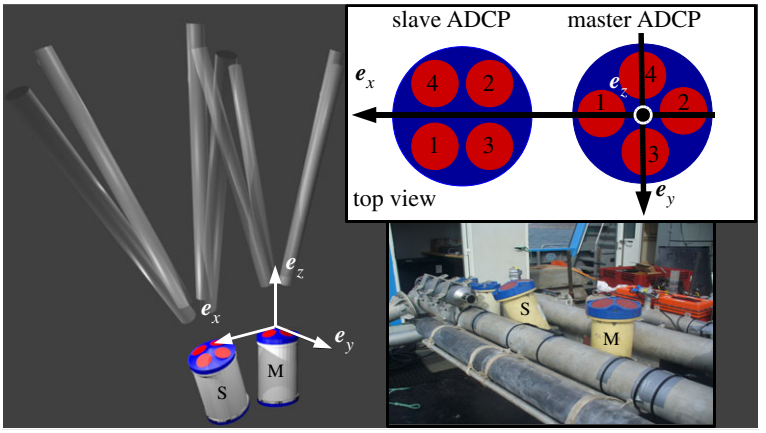

Figure 2. Three-dimensional view of the experimental set-up (left-hand side) with the top view enclosed on the right-hand side. The letters 'S' and 'M' stand for slave and master ADCP respectively. The Cartesian coordinates system is defined relative to the master with the origin located at the centre of the four transducers (red circles). The beam numbering is shown in the $\boldsymbol{e_x}$-$\boldsymbol{e_y}$ plane in the upper right-hand side panel. A photograph of the experimental set-up before the deployment is also enclosed. (Online version in colour.)

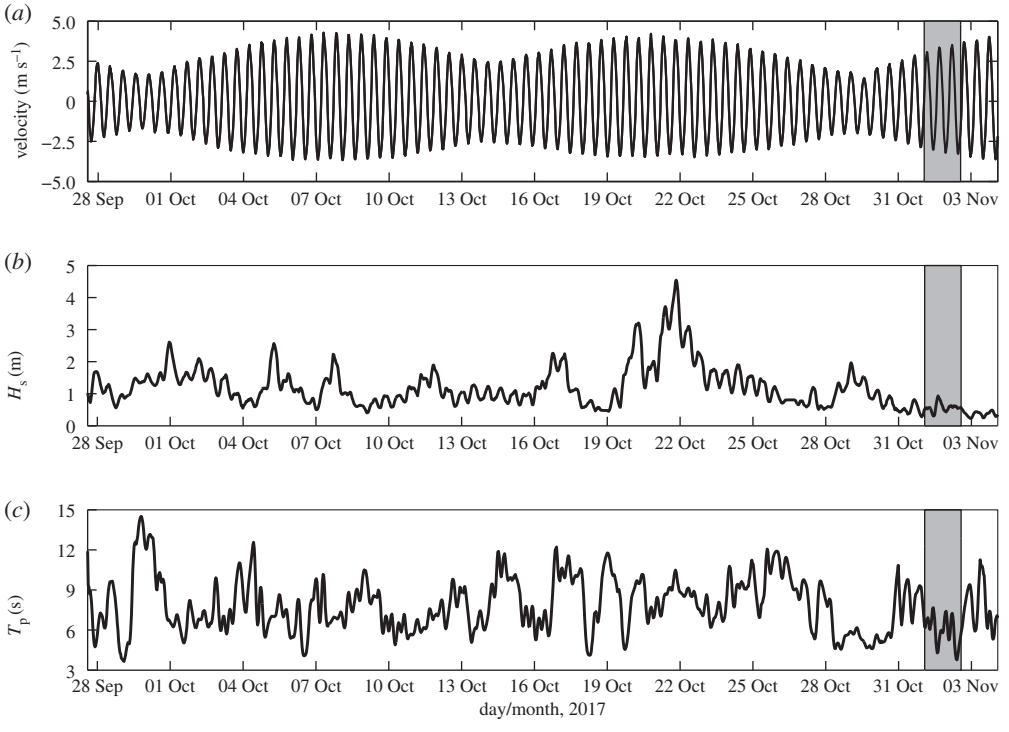

Figure 3. Time series (30 min averaged) of the depth-averaged flow speed (*a*), significant wave height (*b*) and peak period (*c*) computed from the master ADCP measurements. The grey region shows the 36 h long period chosen for turbulence characterization.

Figure 4 confirms this point. The total energy spectrum S_T of the along-beam velocities (equation (2.10)) were computed at different height above bottom within 10 min temporal windows during the 36 h period. Figure 4 shows the mean spectrum at five different depths. At $z = 25$ metre above bottom (m.a.b.), during both flood and ebb tide, the spectrum exhibits a hump extended from 0.09 Hz to 0.14 Hz and centred on 0.12 Hz which corresponds to the mean peak

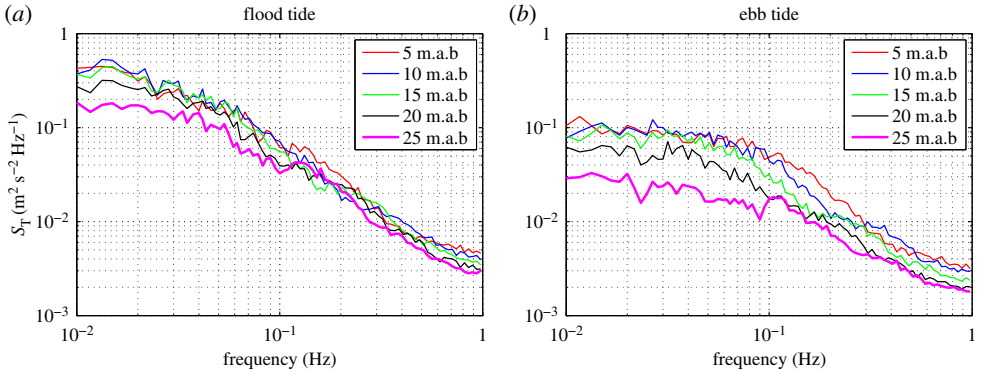

Figure 4. Spectrum resulting from the averaging of the total energy spectra S_T of the along-beam velocities recording during the 36 h long period at different height above bottom on flood (*a*) and ebb (*b*) tide. (Online version in colour.)

wave frequency (T_p) estimated during the 36 h period. This effect remains within the 10 m thick uppermost surface layer. Thus, a clear wave-induced contamination is expected when estimating turbulence within this water layer. Spectra computed at height above bottom lower than 20 m did not exhibit any wave contamination. Further information regarding the spectra can be found in [20].

The 10 m thick uppermost surface layer was not considered in this study. Note that, within the selected period, the wave parameters H_s and T_p are modulated by the semi-diurnal variation of the tide (figure 3*b*,*c*). This effect is explained by the refraction of waves over the tidal currents (e.g. [32]).

(c) Wind conditions

The velocity magnitude, U_W, and the direction, θ_W, of the wind were extracted from the wind-wave model WAVEWATCH III NORGAS-UG (Nord-Gascogne-Unstructured Grid) [32]. The NORGAS-UG configuration is built on a unstructured grid whose meshes range from 10 km spatial resolution up to 200 m off the coast with a time step of 1 h. In the present study, U_W and θ_W time series were extracted at a grid point closest to the location of the ADCPs system (approx. 500 m).

Figure 5 shows the wind rose derived from U_W and θ_W time series recorded during the 36 h long period as well as the direction of the tidal current during flood and ebb tide. During flood tide, the dominant tidal current propagates northeastward whereas during ebb tide the dominant tidal current propagates southwestward. The mean velocity magnitude and direction of the wind were found to be 4.9 m s^{-1} and 227° from north respectively. Two distinct patterns of wind direction were identified. The first pattern exhibits wind propagating from the southeastern direction with θ_W values ranging from 150° and 180° from north. This pattern is associated with the highest velocity magnitudes and occurred during the first 20 h of the 36 h long period. On average, the angle between the wind propagation direction associated with the first pattern and the direction of the dominant tidal current was found to be 135° during flood tide and 45° during ebb tide. The second pattern reveals an opposite propagation direction of wind. Wind propagated from the northwestern direction with θ_W values ranging from 270° and 320° from north. The angle between the wind associated with the second pattern and tidal current direction was found to be around 90° during both flood and ebb phases of the tide.

(d) Analysis techniques

The selected 36 h long period was divided into 226 subsets of 10 min each. Hereafter, an overbar is used to represent a temporal average over each subset. The 10 min duration is of sufficient

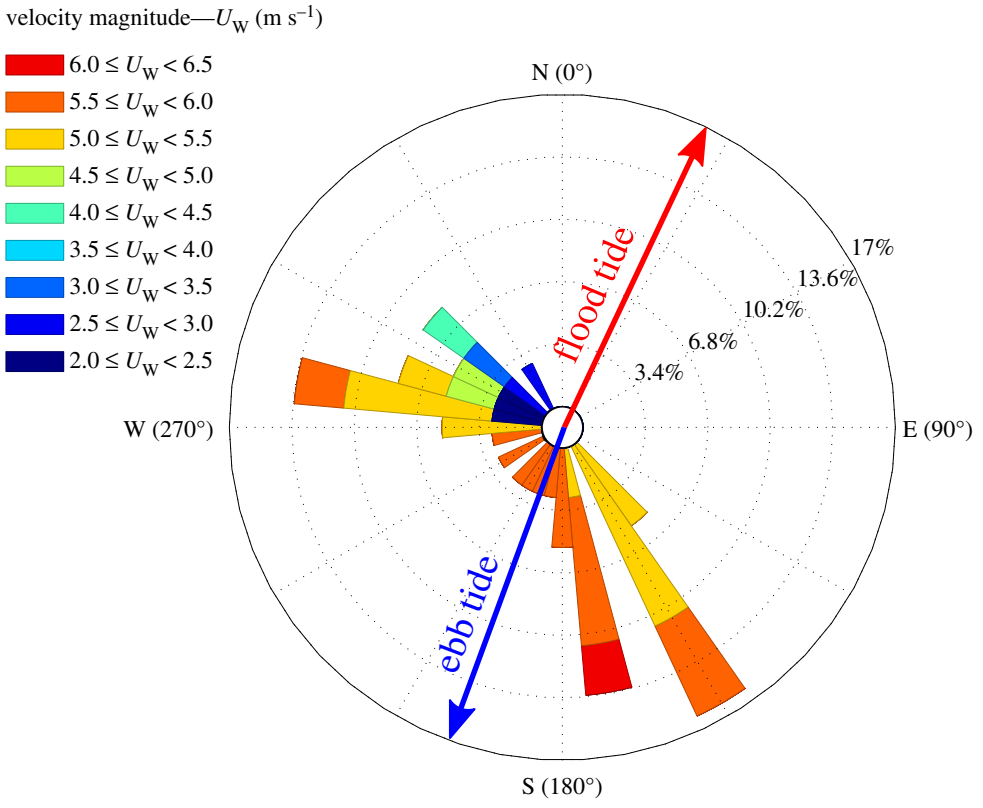

Figure 5. Wind rose observed between 1 November 2017—01.45 UTC and 2 November 2017—13.45 UTC. Occurrences of wind direction are shown in percentage. Red and blue arrows show the direction of the dominant tidal current during flood and ebb tide respectively. (Online version in colour.)

length to provide a good sample of the largest turbulent eddies, but not so long that the turbulent processes cannot be regarded as quasi-stationary. Moreover, since velocity time series are dominated by variability at the semidiurnal frequency (figure 3*a*), a sample length of 10 min is a reasonable compromise between statistical reliability and stationarity. The Reynolds stresses, the TKE dissipation rate and the TKE production rate associated with their uncertainty of measurements were quantified. The analysis techniques used to estimate these turbulence metrics are presented below.

(i) Doppler noise

The fluctuating velocity recorded by an ADCP along each beam is the sum of a true turbulent velocity and an uncertainty associated with Doppler noise. This uncertainty is regularly approximated as Gaussian white noise (e.g. [12,15,20,33,34]) with variance $\sigma^2_{N_I}$ given by

$$\sigma^2_{N_I} = f_N \times N_I, \tag{2.1}$$

where f_N is the Nyquist frequency and N_I is a constant spectral density associated with the energy spectrum S_I of the velocity recorded along the Ith beam.

In our study, $\sigma^2_{N_I}$ was estimated from the velocity measurements of the four-beam master ADCP. Using Taylor's assumption of frozen turbulence, the total variance σ^2_N is given by

$$\sigma^2_N = \frac{U}{2\pi} \sum_{I=1}^{4} \sigma^2_{N_I}, \tag{2.2}$$

where U is the mean flow speed.

(ii) Vertical shear

The vertical gradients of the streamwise, spanwise and vertical velocity, $\partial\overline{u}/\partial z$, $\partial\overline{v}/\partial z$ and $\partial\overline{w}/\partial z$ respectively, were estimated from the master ADCP measurements. The uncertainty σ_S in the shear estimates was calculated such that [12,35]

$$\sigma_S^2 = \frac{\sigma_N^2}{M\Delta z^2 \sin^2 2\theta}, \tag{2.3}$$

where M is the number of samples contained within each 10 min subset (1200 measurement points in this study), $\Delta z = 1.3$ m is the bin size and $\theta = 20^\circ$ is the beam inclination angle.

(iii) Variance Method for coupled ADCPs

The coupled ADCPs method developed by Vermeulen *et al.* [26] combines (i) the traditional transformation method, where two opposite beams of the ADCP are used to transform velocities in beam coordinates to velocities in Cartesian coordinates system, with (ii) the rotation of the slave relative to the master ADCP. The velocities in beam coordinates equates to the velocities (u, v, w) in Cartesian coordinates as

$$\boldsymbol{b} = T\mathbf{u}, \tag{2.4}$$

where $\boldsymbol{b}$ is an eight-component vector containing all the radial velocity components from the two coupled ADCPs, $\mathbf{u}$ is the velocity vector in the Cartesian coordinates system ($\mathbf{u} = u\boldsymbol{e_x} + v\boldsymbol{e_y} + w\boldsymbol{e_z}$) and T is the transformation matrix given in appendix A. The velocities in the Cartesian coordinates system are obtained by inverting the transformation matrix T. Note that T depends on the instruments used and the relative rotation of the slave ADCP.

In order to obtain the components of the Reynolds stress tensor from the velocity variances in beam coordinates, a new eight by six matrix Q is computed. Q results from the product of the terms in T such that

$$Q = T_{p,q}T_{p,m}, \tag{2.5}$$

where $p = [1;8]$ and $q,m = [1;3]$. Q allows relating the vector $\boldsymbol{v_b}$, containing the velocity variances in beam coordinates to the vector $\boldsymbol{r}$ containing the six terms of the Reynolds stress tensor as

$$\boldsymbol{v_b} = Q\boldsymbol{r}. \tag{2.6}$$

The six-element vector $\boldsymbol{r}$ can be rearranged to form the Reynolds stress tensor according to

$$\mathbf{R} = \begin{pmatrix} r_1 & r_4 & r_5 \\ r_4 & r_2 & r_6 \\ r_5 & r_6 & r_3 \end{pmatrix} = \begin{pmatrix} \overline{u'^2} & \overline{u'v'} & \overline{u'w'} \\ \overline{u'v'} & \overline{v'^2} & \overline{v'w'} \\ \overline{u'w'} & \overline{v'w'} & \overline{w'^2} \end{pmatrix}. \tag{2.7}$$

The prime denotes a fluctuation from the mean.

The uncertainty $\sigma_{R_{p,n}}$ in the Reynolds stress estimates is given by [26]

$$\sigma_{R_{p,n}}^2 = \frac{2}{M}\sum_{p=1}^{8}\left(Q_{p,n}^{+}v_{b_p}\right)^2 \quad (n = 1,\ldots,6), \tag{2.8}$$

where $Q^+ = (Q^{\mathrm{T}}Q)^{-1}Q^{\mathrm{T}}$ with Q^{T} being the transpose of Q and v_{b_p} is the magnitude of the velocity vector $\boldsymbol{v_b}$, recorded along the pth beam.

(iv) TKE dissipation and production rate

The TKE dissipation rate ε is estimated from the spectral method [11,12,20]. This method requires the observation of an inertial subrange in which the energy spectra S_I of the velocity recorded along the Ith beam follow the classic $-5/3$ slope as a manifestation of the energy cascade [36,37]. In our analysis, only the energy spectra of the along-beam velocities recorded by the four-beam

master ADCP are considered. Using Taylor's assumption of frozen turbulence, the total energy spectrum S_T of the velocity can be given by

$$S_T = \frac{U}{2\pi}\sum_{I=1}^{4} S_I. \tag{2.9}$$

Under negligible wave motions, the total energy spectrum $S_T(k)$ can be related to the TKE dissipation rate ε and the radian wavenumber k such that

$$S_T(k) = C\varepsilon^{2/3}k^{-5/3} + N_T, \tag{2.10}$$

where $C \approx 1.5$ is the universal Kolmogorov constant and N_T is the summed Doppler noise level such that

$$N_T = \frac{U}{2\pi}\sum_{I=1}^{4} N_I. \tag{2.11}$$

The TKE dissipation rate ε can then be expressed as

$$\varepsilon = C^{-3/2}\langle X\rangle^{3/2}, \tag{2.12}$$

where $X = (S_T - N_T)k^{5/3}$ and the brackets denote an average over the inertial subrange.

The uncertainty σ_ε in the TKE dissipation rate estimates is calculated by propagating the uncertainty in X calculation such that

$$\sigma_\varepsilon = \frac{3}{2}C^{-3/2}\langle X\rangle^{1/2}\sigma_X, \tag{2.13}$$

where σ_X is the variance of X in the range of frequencies covering the inertial subrange.

Evaluation of the TKE budget is useful to understand the dynamics of the turbulence of a tidal flow. The full TKE budget can be written as [37]

$$\frac{1}{2}\frac{\mathrm{d(TKE)}}{\mathrm{d}t} = T_p + T_d + \mathcal{P} - \varepsilon, \tag{2.14}$$

where the rate of change of TKE is equal to the sum of a pressure transport term T_p, a diffusive transport term T_d, the TKE production rate $\mathcal{P}$ and the TKE dissipation rate ε. All terms in equation (2.14) are obtained from our measurements, with the exception of the pressure transport term

$$T_p = -\frac{1}{\rho_0}\frac{\partial}{\partial z}\overline{p'w'}, \tag{2.15}$$

where p is the pressure and ρ_0 is the seawater density. T_p cannot be estimated from our measurements.

The diffusive transport term T_d is estimated from the vertical gradient of the TKE vertical flux F such that

$$T_d = -\frac{\partial F}{\partial z} \quad \text{with } F = \frac{1}{2}\overline{w'q^2}. \tag{2.16}$$

At highly energetic and well-mixed sites, such that of the present study, the time derivative as well as the pressure transport and diffusive terms are usually negligible; thus, an assumption of local equilibrium is commonly made such that $\varepsilon \approx \mathcal{P}$ (e.g. [12,15,38,39]). This assumption will be tested in this study.

The TKE production rate $\mathcal{P}$ indicates the amount of energy that is transferred from the mean flow to the TKE. $\mathcal{P}$ is estimated from the product of the Reynolds stresses and the vertical gradient of the streamwise, spanwise and vertical velocity as

$$\mathcal{P} = -\left(\overline{u'w'}\frac{\partial\overline{u}}{\partial z} + \overline{v'w'}\frac{\partial\overline{v}}{\partial z} + \overline{w'^2}\frac{\partial\overline{w}}{\partial z}\right). \tag{2.17}$$

The uncertainty $\sigma_{\mathcal{P}_{i,j}}$ associated with the TKE production rate generated by the Reynolds stress $\overline{u_i'u_j'}$ and the gradient $\partial\overline{u_i}/\partial x_j$ can be determined using the formula for the variance of a product

such that [35]

$$\sigma^2_{\mathcal{P}_{i,j}} = \overline{u_i' u_j'}^2 \sigma_S^2 + \frac{\partial \overline{u_i}}{\partial x_j} \sigma_R^2 + \sigma_S^2 \sigma_R^2. \tag{2.18}$$

Equations (2.17) and (2.18) are combined to provide the total uncertainty $\sigma_{\mathcal{P}}$ of the TKE production rate

$$\sigma_{\mathcal{P}} = \sqrt{\sigma^2_{\mathcal{P}_{uw}} + \sigma^2_{\mathcal{P}_{vw}} + \sigma^2_{\mathcal{P}_{ww}}}. \tag{2.19}$$

3. Results

(a) Reynolds stresses

Time series of the six components of the Reynolds stress tensor were computed at $z = 5$ m.a.b. and $z = 18$ m.a.b.. Figure 6 shows that the magnitude of the normal and shear stresses are modulated by tidal currents with maximum values reached at peak flood and ebb tide velocity. Globally, the magnitude of the Reynolds stresses decreases with the increasing height above bottom. The component $\overline{u'^2}$ has the highest magnitude of the Reynolds stress tensor. The mean value $\langle \overline{u'^2} \rangle$ averaged over the flood and ebb stage of the tide was found to be $7.7 \times 10^{-2}\,\mathrm{m^2\,s^{-2}}$ and $7.05 \times 10^{-2}\,\mathrm{m^2\,s^{-2}}$ at $z = 5$ m.a.b. (table 1). Upper in the water column, at $z = 18$ m.a.b., $\langle \overline{u'^2} \rangle$ decreases significantly and reaches $5.0 \times 10^{-2}\,\mathrm{m^2\,s^{-2}}$ and $2.8 \times 10^{-2}\,\mathrm{m^2\,s^{-2}}$ during flood and ebb tide respectively. The component $\langle \overline{v'w'} \rangle$ is the lowest magnitude of the Reynolds stresses. The ratio $\langle \overline{u'^2} \rangle / \langle \overline{v'w'} \rangle$ was found to be up to 22 during flood tide and up to 35 during ebb tide.

During flood tide, both normal stresses, $\langle \overline{v'^2} \rangle$ and $\langle \overline{w'^2} \rangle$, and both shear stresses $\langle \overline{u'v'} \rangle$ and $\langle \overline{u'w'} \rangle$ were found to be of the same order of magnitude, typically $2\text{–}3 \times 10^{-2}\,\mathrm{m^2\,s^{-2}}$ at $z = 5$ m.a.b. and $1\text{–}2 \times 10^{-2}\,\mathrm{m^2\,s^{-2}}$ at $z = 18$ m.a.b. (table 1). During ebb tide, $\langle \overline{v'^2} \rangle$ and $\langle \overline{w'^2} \rangle$ values vary little in comparison to that obtained during the flooding stage of the tide and their values are similar at $z = 5$ m.a.b. and $z = 18$ m.a.b.. The shear stresses exhibit different features. Significant difference was found when comparing their magnitude during flood and ebb tide. On ebb tide, $\langle \overline{u'v'} \rangle$ is up to four times lower than during flood tide.

The ratios $\sigma_{R_{u_i u_j}} / \langle \overline{u_i u_j} \rangle$ were investigated. Globally, the ratios increase with height above bottom (table 2). The only exception is $\sigma_{R_{ww}} / \langle \overline{w'^2} \rangle$, which is higher at $z = 5$ m.a.b. than at $z = 18$ m.a.b.. The ratios associated with the normal stresses are higher during flood tide than during ebb tide whereas the opposite is exhibited for the shear stresses. Another remarkable feature is that the highest ratios are associated with the velocity fluctuation v' of the spanwise velocity v (table 2).

(b) TKE budget

(i) Estimates of the TKE dissipation and production rates

Time series of the TKE dissipation rate ε and production rate $\mathcal{P}$ are shown in figure 7. Both turbulence metrics track each other and exhibit a clear tidal variation. Maximum values of ε and $\mathcal{P}$ are observed during peak flood tide velocity, falling off around slack water and increasing to a second maximum during peak ebb tide velocity. At $z = 5$ m.a.b., the TKE dissipation rates averaged over flood and ebb tide are close to each other: $3.2 \times 10^{-3}\,\mathrm{m^2\,s^{-3}}$ and $3.0 \times 10^{-3}\,\mathrm{m^2\,s^{-3}}$ respectively. The TKE production rate exhibits a slight asymmetry with a mean value of $2.4 \times 10^{-3}\,\mathrm{m^2\,s^{-3}}$ during flood tide and $1.8 \times 10^{-3}\,\mathrm{m^2\,s^{-3}}$ during ebb tide. The gap between the mean of ε and $\mathcal{P}$ is due to very low values of the TKE production rates during periods of low tidal velocity (less than $1\,\mathrm{m\,s^{-1}}$), during which $\mathcal{P}$ is up to four times lower than ε whereas both turbulence metrics are of the same order of magnitude during peak tidal velocity. At $z = 18$ m.a.b., significant asymmetries between values of ε as well as $\mathcal{P}$ observed during flood and ebb tide are exhibited. During flood tide, $\varepsilon = 1.6 \times 10^{-3}\,\mathrm{m^2\,s^{-3}}$ and $\mathcal{P} = 0.6 \times 10^{-3}\,\mathrm{m^2\,s^{-3}}$ on average, whereas during ebb tide those values are respectively two and three times lower. Moreover, the

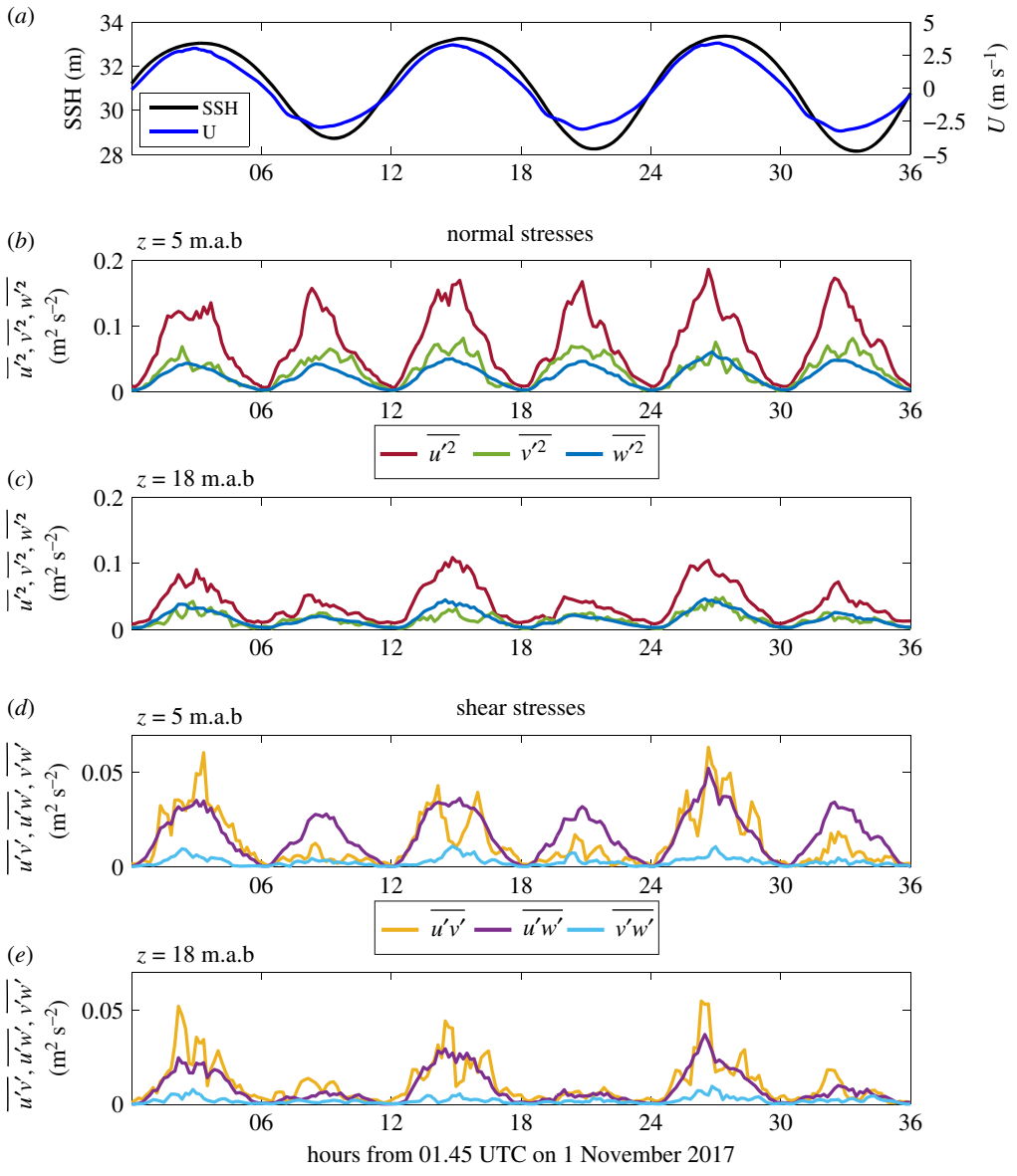

Figure 6. Time series of the normal stresses (*b*,*c*) and the shear stresses (*d*,*e*) computed at $z = 5$ m.a.b. (*b*,*d*) and $z = 18$ m.a.b. (*c*,*e*) during the 36 h long period used for turbulence characterization. Time series of the sea surface height (SSH) and depth-averaged tidal velocity are shown in (*a*) by black and blue colour respectively. (Online version in colour.)

TKE dissipation rate is constantly higher than the TKE production rate. Minimum gaps between ε and $\mathcal{P}$ values are reached during peak velocity whereas maximum gaps are exhibited during periods of low tidal velocity.

Speed bin-averaged vertical profiles of ε and $\mathcal{P}$ were computed using the depth-averaged flow speed to sort the data (figure 8). Globally, both parameters decrease with height above the seabed. However, a slight increase of the TKE production rate is observed at height above bottom higher than 18 m, particularly for the vertical profile associated with the depth-averaged flow speed of $1.5\,\mathrm{m\,s^{-1}}$ (figure 8*b*). This observation is a result of the corruption of the Reynolds stresses estimates by noise, which has been identified to be associated with the wave orbital velocities

Table 1. Mean Reynolds stresses $\langle\overline{u_i u_j}\rangle$ associated with their uncertainty $\sigma_{R_{u_i u_j}}$ (equation (2.8)), averaged over the flood and ebb tidal conditions during the 36 h long period at $z = 5$ m.a.b. and $z = 18$ m.a.b.. The unit is 10^{-2} m^2 s^{-2}.

		$\langle\overline{u'^2}\rangle \pm \sigma_{R_{uu}}$	$\langle\overline{v'^2}\rangle \pm \sigma_{R_{vv}}$	$\langle\overline{w'^2}\rangle \pm \sigma_{R_{ww}}$	$\langle\overline{u'v'}\rangle \pm \sigma_{R_{uv}}$	$\langle\overline{u'w'}\rangle \pm \sigma_{R_{uw}}$	$\langle\overline{v'w'}\rangle \pm \sigma_{R_{vw}}$
flood tide	$z = 5$ m.a.b.	7.7 ± 0.6	3.05 ± 1.0	2.6 ± 0.1	2.1 ± 0.7	2.0 ± 0.1	0.35 ± 0.1
	$z = 18$ m.a.b.	5.0 ± 0.5	1.7 ± 0.75	2.1 ± 0.1	1.7 ± 0.5	1.3 ± 0.1	0.25 ± 0.1
ebb tide	$z = 5$ m.a.b.	7.05 ± 0.5	3.6 ± 0.7	2.3 ± 0.1	0.5 ± 0.35	1.4 ± 0.15	0.2 ± 0.1
	$z = 18$ m.a.b.	2.8 ± 0.2	1.2 ± 0.35	1.1 ± 0.1	0.5 ± 0.2	0.35 ± 0.05	0.1 ± 0.05

royalsocietypublishing.org/journal/rsta *Phil. Trans. R. Soc. A* **378**: 20190496

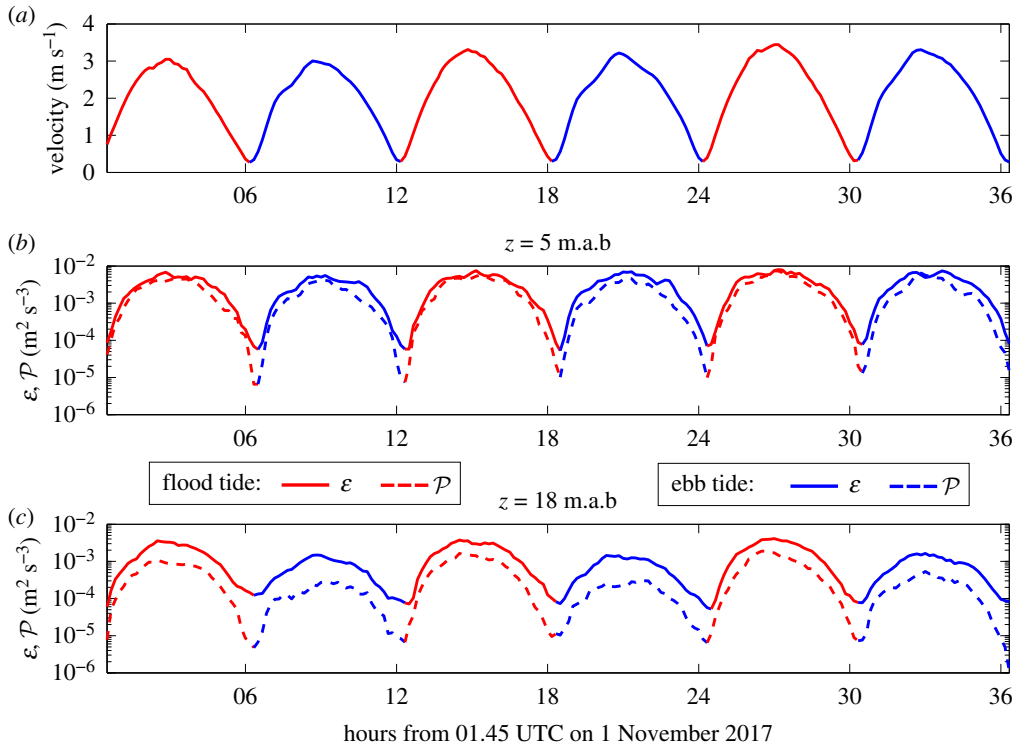

Figure 7. Time series of the TKE dissipation rate ε (solid line) and production rate $\mathcal{P}$ (dashed line) computed at $z = 5$ m.a.b. (*b*) and $z = 18$ m.a.b. (*c*) during the 36 h long period used for turbulence characterization. Time series of the depth-averaged tidal velocity magnitude is given in (*a*). Red and blue colours are used to identify the flooding and ebbing stages of the tide respectively. (Online version in colour.)

Table 2. Mean ratios $\sigma_{R_{u_iu_j}} / \langle \overline{u_i u_j} \rangle$ in percentage (%) obtained on flood and ebb tide during the 36 h long period at $z = 5$ m.a.b. and $z = 18$ m.a.b..

		$\sigma_{R_{uu}} / \langle \overline{u'^2} \rangle$	$\sigma_{R_{vv}} / \langle \overline{v'^2} \rangle$	$\sigma_{R_{ww}} / \langle \overline{w'^2} \rangle$	$\sigma_{R_{uv}} / \langle \overline{u'v'} \rangle$	$\sigma_{R_{uw}} / \langle \overline{u'w'} \rangle$	$\sigma_{R_{vw}} / \langle \overline{v'w'} \rangle$
flood tide	$z = 5$ m.a.b.	8	33	4	33	5	29
	$z = 18$ m.a.b.	10	44	5	29	8	40
ebb tide	$z = 5$ m.a.b.	7	19	4	70	11	50
	$z = 18$ m.a.b.	7	29	9	40	14	50

resulting from the slightly stronger surface wave activity during events on the ebbing stage of the tide where the peak wave periods were higher than 8 s.

The ratio of the rates of dissipation to production of turbulent kinetic energy has been calculated. The quantitative comparison between ε and $\mathcal{P}$ was made by calculating the individual ratios of ε with the corresponding values of $\mathcal{P}$. Vertical profiles of $\varepsilon/\mathcal{P}$ are shown in figure 8*c*. Globally, $\varepsilon/\mathcal{P} > 1$ throughout the water column, indicating that TKE dissipation exceeds TKE production. The ratios increase with height above bottom reaching a maximum at mid-depth (15–18 m) and then decreasing slightly because of increasing TKE production rates. The ratios were found to be increasing with decreasing flow speed. Ratios associated with the depth-averaged flow speed of 1.5 m s^{-1} and 3.5 m s^{-1} exhibit a maximum of 3.8 and 2.4 respectively at $z = 18$ m.a.b.. Minimum ratios were found near the seabed

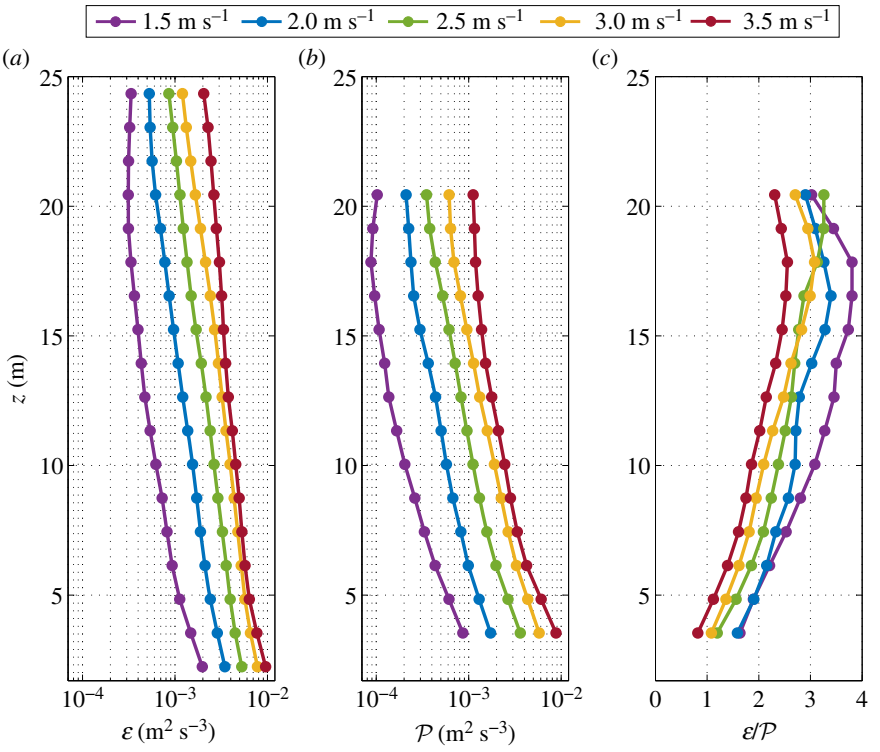

Figure 8. TKE dissipation rate ε (*a*), TKE production rate $\mathcal{P}$ (*b*) and ratio $\varepsilon/\mathcal{P}$ (*c*) as a function of height above bottom. Profiles have been averaged into 0.5 m s^{-1} speed bins based on the depth-averaged flow speed. (Online version in colour.)

($z = 3.5$ m.a.b.), where the frictional forces are the strongest. There, $\varepsilon/\mathcal{P}$ ranges between 0.9 and 1.8.

(ii) Uncertainties in TKE dissipation and production rates estimates

Uncertainties σ_ε and $\sigma_\mathcal{P}$ when estimating respectively the TKE dissipation and production rate were evaluated (equations (2.13) and (2.19)). Figure 9 shows the variation of $\varepsilon \pm \sigma_\varepsilon$ and $\mathcal{P} \pm \sigma_\mathcal{P}$ throughout the water column during flood and ebb tide. On flood tide, the depth-averaged TKE dissipation and production rate were found to be $(2.2 \pm 0.35) \times 10^{-3}$ m^2 s^{-3} and $(1.2 \pm 0.3) \times 10^{-3}$ m^2 s^{-3} respectively. On ebb tide, the TKE dissipation and production rate are 30% lower: $(1.6 \pm 0.2) \times 10^{-3}$ m^2 s^{-3} and $(0.8 \pm 0.25) \times 10^{-3}$ m^2 s^{-3} respectively.

In figure 9, the uncertainties in ε and $\mathcal{P}$ estimates are identified by the spread (shading colour) from the mean profiles (solid lines) of the TKE dissipation and production rates. Higher uncertainties are associated with higher spreading. During flood tide, the uncertainty in ε and $\mathcal{P}$ estimates slightly increases with height above bottom. During ebb tide, the uncertainty associated with $\mathcal{P}$ estimates exhibits similar feature but with significant spreading from the mean profile whereas the uncertainty associated with ε estimates increases until a maximum at $z = 10$ m.a.b. and then slightly decreases until a minimum at $z = 20.4$ m.a.b..

The ratios $\sigma_\varepsilon/\varepsilon$ and $\sigma_\mathcal{P}/\mathcal{P}$ were investigated. Both ratios exhibited opposite trend regarding the stage of the tide. The depth-averaged value of $\sigma_\varepsilon/\varepsilon$ was found to be higher during flood tide than during ebb tide with respective values of 17% and 10% whereas the depth-averaged value of $\sigma_\mathcal{P}/\mathcal{P}$ was found to be lower during flood tide than during ebb tide with respective values of 29% and 44%. Very high values of $\sigma_\mathcal{P}/\mathcal{P}$ were found during the ebbing stage of the tide, specially in the uppermost part of the water column where $\sigma_\mathcal{P}/\mathcal{P}$ reaches its maximum value of 86% at $z = 20.4$ m.a.b..

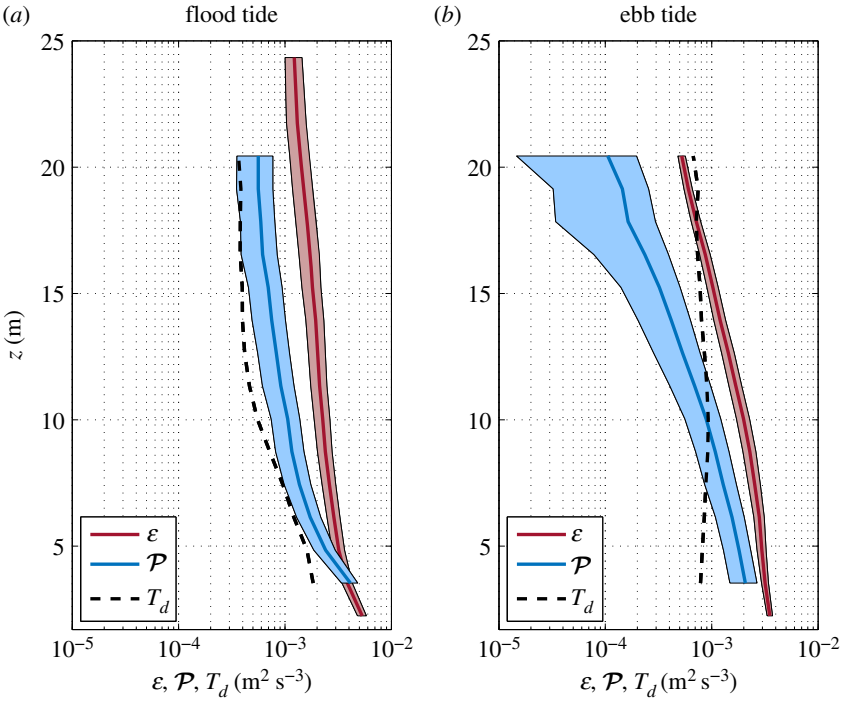

Figure 9. Vertical profiles of the TKE dissipation rate, ε (red), TKE production rate, $\mathcal{P}$ (blue) and the diffusive transport of TKE, T_d (black dashed line) averaged over flooding (*a*) and ebbing (*b*) stages of the tide. Red and blue shading are used to identify the uncertainty σ_ε and $\sigma_\mathcal{P}$ respectively from the mean value of ε and $\mathcal{P}$ (solid lines). (Online version in colour.)

(c) Estimates of the diffusive transport of TKE

The estimation of the diffusive transport of TKE, T_d, together with the TKE dissipation and production rate allows for the comparison of the relative importance of different terms in the TKE budget. The local imbalance between ε and $\mathcal{P}$ implies that other terms in the TKE equation, such as T_d, must be significant. Vertical variation of T_d averaged over both flood and ebb tide are given in figure 9. The depth-averaged value of T_d was found to be slightly higher during ebb tide than during flood tide: $0.8 \times 10^{-3}\,\mathrm{m^2\,s^{-3}}$ and $0.7 \times 10^{-3}\,\mathrm{m^2\,s^{-3}}$ respectively. On average, $\mathcal{P}$, ε and T_d were found such that (i) $\mathcal{P} = 1.5T_d$ and $\varepsilon = 3T_d$ during flood tide, and (ii) $\mathcal{P} \sim T_d$ and $\varepsilon = 2T_d$ during ebb tide.

Above $z \sim 10$ m.a.b., T_d is almost constant for both flood and ebb tide whereas below $z \sim 10$ m.a.b.., T_d variation with depth exhibits opposite behaviour depending on the tidal stage. During flood tide, T_d decreases with height above bottom with a negative slope indicating that TKE is exported. However, during ebb tide, T_d increases with height above bottom with a positive slope indicating that TKE is imported. During flood tide, T_d is constantly lower than the production rate $\mathcal{P}$ and the dissipation rate ε with the tendency that $T_d < \mathcal{P} < \varepsilon$. During ebb tide, the water column can be split into three depth ranges: (i) $z < 10$ m.a.b., where $T_d < \mathcal{P} < \varepsilon$, (ii) 10 m.a.b. $< z <$ 18 m.a.b., where $\mathcal{P} < T_d < \varepsilon$, and (iii) $z >$ 18 m.a.b., where $\mathcal{P} < \varepsilon < T_d$.

4. Discussion

Knowledge of both the water column structure and momentum is critical for shelf sea circulation models to have an accurate representation of the vertical transfers due to turbulent diffusion.

These models treat turbulence explicitly for parametrization of sub-grid scale vertical mixing processes with turbulence closure schemes. These schemes involve explicit representations of the evolution of TKE including its production due to shear stress and buoyancy and its dissipation through which energy is converted to heat. Testing these turbulence closure schemes through the use of reliable turbulence measurements is a necessity. It will allow for properly adjusting the numerical models and, thus, improve their ability to reproduce the flow dynamics.

In this paper, we present what we believe to be the first series of simultaneous and independent measurements of the TKE dissipation rate ε and the TKE production rate $\mathcal{P}$, covering a large proportion of the water column at a highly energetic site in the Alderney Race. Both turbulence metrics were found to closely track each other and follow a quarter-diurnal pattern. Similarly to numerous previous studies (e.g. [9,10,12,15,22,38,39]), the ratio $\varepsilon/\mathcal{P}$ exhibited significant deviation from the expected value of unity. The ratio was found to be higher than 1 throughout the water column suggesting that TKE dissipation exceeds TKE production. The mean depth-averaged value of $\varepsilon/\mathcal{P}$ during flood and ebb tide were found to be 2.2 and 2.8 respectively. These different values suggest that both TKE dissipation and production are governed by bathymetry features. The minimum ratio was found near the seabed, during the most energetic periods ($U > 2\,\mathrm{m\,s^{-1}}$) where an equilibrium state ($\varepsilon \approx \mathcal{P}$) was achieved. During less energetic conditions ($U < 1.5\,\mathrm{m\,s^{-1}}$), $\varepsilon/\mathcal{P}$ reaches a maximum at mid-depth suggesting that the transport of TKE is of importance during such conditions.

The transport of TKE involves two quantities: the pressure transport T_p and the diffusive transport T_d. The latter has been estimated during both flood and ebb tide. Significant values of T_d were found for both tidal stages. In particular, T_d calculated within the uppermost part of the water column during ebb tide was found to be the dominant term of the TKE budget. This result shows that the diffusive transport is important to the TKE budget and the common assumption of a local balance (i.e. a balance between production and dissipation) is not valid at our measurement site. Moreover, we expect that the pressure transport term T_p is required to close the TKE budget, particularly near the surface.

The transport of TKE is not the only reason that might explain such gap from the local $\mathcal{P} - \varepsilon$ balance. We suspect that either the TKE production rate estimated using the variance method is underestimated, or that the TKE dissipation rate computed from the spectra of the along-beam velocities is too large. In order to evaluate the source of error when estimating the TKE dissipation and production rate, their respective uncertainty σ_ε and $\sigma_\mathcal{P}$ have been computed.

The source of error in ε estimates originates, only, in the calculation of the variance of $(S_T - N_T)k^{5/3}$ calculated within the range of frequencies covering the inertial subrange (equation (2.13)). Since N_T is a constant, the only contribution in the variance calculation derives from the total energy spectrum S_T of the along-beam velocity recorded by the master ADCP. On average the variance of S_T was found to be only 3%. This explains the low depth-averaged value of $\sigma_\varepsilon/\varepsilon$ of 10% during ebb tide and 17% during flood tide. As a result, we feel relatively confident in our estimates of the TKE dissipation rate.

The likely error increasing the deviation from the expected unity is a bias in $\mathcal{P}$ estimates. The ratio $\sigma_\mathcal{P}/\mathcal{P}$ was found to be three times higher than $\sigma_\varepsilon/\varepsilon$. The source of error in the estimation of the TKE production rate is twofold. It depends on both σ_R and σ_S, the uncertainty in the Reynolds stresses and the shear estimates respectively (equation (2.18)). The calculation of the TKE production rate involves three components of the Reynolds stress tensor: $\overline{u'w'}$, $\overline{v'w'}$ and $\overline{w'^2}$. The uncertainties, $\sigma_{R_{uw}}$, $\sigma_{R_{vw}}$ and $\sigma_{R_{ww}}$, in their estimation, are of similar magnitude and relatively constant throughout the water column, typically $1.0 \times 10^{-3}\,\mathrm{m^2\,s^{-2}}$ on average (table 1). The depth-averaged value of σ_S was found to be twice higher: $2.0 \times 10^{-3}\,\mathrm{m^2\,s^{-2}}$. Moreover, similarly to the uncertainty in $\mathcal{P}$ estimates, σ_S increases with height above bottom. This result suggests that $\sigma_\mathcal{P}$ variation throughout the water column is governed by σ_S.

It is readily seen from the expression of σ_S (equation (2.3)) that the uncertainty in the shear and, thus, the uncertainty in $\mathcal{P}$ estimates can be reduced by increasing the number M of points to be averaged. In our study, this number was set to 1200 points which corresponds to a time

interval of 10 min. The duration of this averaging period is commonly used for turbulence characterization since it allows retaining the longest timescales of coherent turbulence structures in the velocity fluctuation, while capturing the tidal and semi-diurnal variations in the mean flow speed [16,20,38]. σ_S might also be reduced by increasing the bin size Δz, at the expense of the vertical resolution. However, because of the finite ADCP pulse length, eddies smaller than twice the range bin size cannot be resolved. As a consequence, the main disadvantage of increasing the bin size is that it will severely limit the lengthscales of turbulent motions that can be captured.

The 36 h long period selected for the turbulence analysis was specifically chosen so as to avoid the turbulence measurements to be contaminated by wave-induced effects. However, surface wave occurrences were identified by the presence of a peak in the along-beam velocity spectra in a wave band interval of frequency $\in [0.09, 0.14]$ Hz. High variances over this frequency interval were observed during most strong ebb tides when the southward tidal current direction opposed the propagation of the most dominant waves [10,20]. During such events, high values of σ_R were exhibited, specifically in the upper layer of the water column ($z > 15$ m.a.b.). As a result, significant uncertainties in the calculation of the TKE production rate were found with a value of $\sigma_{\mathcal{P}}/\mathcal{P}$ reaching 83% at $z = 20.4$ m.a.b. (figure 9*b*).

In our study, two four-beam ADCPs were coupled in a master–slave configuration following the method proposed by Vermeulen *et al.* [26]. The eight-beam set-up allows resolving the six components of the Reynolds stress tensor. Our study showed that the two lowest magnitudes of the Reynolds stresses are $\overline{u'w'}$ and $\overline{v'w'}$. These two terms are the only components that can be estimated from four-beam ADCP measurements. Although such sensors are widely used for turbulence characterization, this result demonstrates that, used alone, four-beam ADCPs do not enable to carry out comprehensive study of turbulence characterization. A better alternative is the use of five-beam ADCP. Such sensors are similar to the conventional four-beam Janus configuration [40] but with the addition of a vertical beam which allows for a true measurement of vertical velocities and the estimation of five components of the Reynolds stress tensor. Five-beam ADCPs have recently become widely available as off-the-shelf instruments. They have been, for instance, successfully used to measure turbulence at two energetic tidal channels within Puget Sound, USA [12]. However, with such an instrument, the horizontal shear stress, $\overline{u'v'}$, remains unknown. Our study shows that the magnitude of this component is significant, in particular during flood tide, its knowledge is thus essential.

Although the eight-beam arrangement enables the full Reynolds stress tensor to be resolved, it has some disadvantages. In upward-looking deployment, ADCPs have a potential for sidelobe contamination which strictly depends on the angle θ between the transducers and the vertical. In the present experiment, ADCPs with angle $\theta = 20^\circ$ were used. With such sensors, the last 6% are contaminated by sidelobes. Thus, measurements performed within only the first 94% of the water column are considered to be valid. When configuring such instruments in a master–slave set-up, the slave ADCP is oriented relative to the master ADCP so that one beam is pointed vertically upward. The typical configuration devised by Vermeulen *et al.* [26] and used in the present study corresponds to yaw $= 45^\circ$ and pitch $= 20^\circ$. Therefore, one of the beams of the slave ADCP is slanted by 40° which reduces the valid range of measurements to the first 77% of the water column. Moreover, Vermeulen *et al.* [26] showed that the yaw and the pitch strongly impact the calculation of the Reynolds stresses. Thus, any uncertainties in the mechanical mount of the two ADCPs induce uncertainties in Reynolds stresses estimates. Another disadvantage is associated with the difficulty of synchronizing the two ADCPs so as to interleave the pings and minimize ping-to-ping interferences. Sending and receiving the synchronizing trigger adds to the signal processing overheads and it is challenging to reach constant sampling of 1–2 Hz within water depths higher than 30–35 m. A valuable alternative to the eight-beam arrangement is the use of seven-beam or eight-beam ADCPs. Similarly to the eight-beam arrangement, such sensors allow resolving the full Reynolds stress tensor but with an easier and cheaper set-up. Such instruments are now available off-the-shelf and might overtake the classic four-beam ADCP and become the preferred choice for conducting turbulence characterization within the next decade.

5. Conclusion

Measurements of two coupled ADCPs were used to quantify the TKE dissipation rate ε and TKE production rate $\mathcal{P}$ throughout a large proportion of the water column at a given location in the Alderney Race. The eight-beam arrangement enabled the evaluation of the six components of the Reynolds stress tensor which allows for an improved estimation of the TKE production rate. Since the Alderney Race is a highly energetic and well-mixed site, it was expected that the TKE dissipation and production would have balanced. However, our results showed that the TKE dissipation strongly exceeds TKE production. The diffusive transport T_d of TKE was found to be significant, in particular during ebb tide where T_d was found to be the most important term of the TKE budget.

Our measurements allow determining all the terms in the TKE budget with the exception of the pressure transport term T_p. It is is expected that this term could be important within the uppermost part of the water column and that its knowledge will close the TKE budget.

It was shown that the significant gap from the expected $\mathcal{P} - \varepsilon$ balance also originated from a likely underestimation of $\mathcal{P}$ estimates. Our results exhibited significant uncertainties when calculating $\mathcal{P}$, in particular during ebb tide. It was strongly suspected that such uncertainties derived from wave-induced effects.

In stratified environmental flows, the interaction between turbulent mixing and the ambient shear and stratification is critical to both predicting the evolution of the flows and the transport of scalars within those flows. Laboratory and numerical studies are effective at isolating processes and provide complete datasets for certain idealized sets of conditions when studying stratified turbulence. However field observations, such as those proposed in this study, are the only way to capture the true complexity of the flows within dynamic environments. We believe that our results will provide the modellers with better information for developing and validating turbulence closure of shelf sea circulation developed to simulate flow dynamics in the Alderney Race.

Data accessibility. This article has no additional data.

Authors' contributions. M.T. performed the analysis and drafted the manuscript. J.-F.F. and G.D. reviewed the paper. C.M. reviewed the paper and provided the data for the wind conditions analysis.R.D. was coordinator of the THYMOTE project. E.D. carried out the experiment. S.G reviewed the paper and was head of the THYMOTE project.

Competing interests. We declare we have no competing interests.

Funding. This work benefited from funding support from France Énergies Marines and the French Government, operated by the National Research Agency under the Investments for the Future program: Reference ANR-10-IEED-0006-11. The study represents a contribution to the THYMOTE (Tidal turbulence: modelling, field observations and tank experiments) project of the above program. We also wishes to acknowledge the financial support from the Strategy for Durable Attractivity (SAD) program managed by the Region Bretagne (Brittany).

Acknowledgements. The skill and experience of Nicolas Chaplain (iXBlue) during the fieldwork are appreciated and acknowledged. We acknowledge our colleague, Professor Alexei Sentchev (ULCO), for his valuable comments on the manuscript.

Appendix A. Transformation matrix

The transformation matrix T is given by

$$T = \begin{pmatrix} \sin\varphi & 0 & \cos\varphi \\ -\sin\varphi & 0 & \cos\varphi \\ 0 & -\sin\varphi & \cos\varphi \\ 0 & \sin\varphi & \cos\varphi \\ 0 & 0 & 0 \\ 0 & 0 & 0 \\ 0 & 0 & 0 \\ 0 & 0 & 0 \end{pmatrix} + \begin{pmatrix} 0 & 0 & 0 \\ 0 & 0 & 0 \\ 0 & 0 & 0 \\ 0 & 0 & 0 \\ \sin\varphi & 0 & \cos\varphi \\ -\sin\varphi & 0 & \cos\varphi \\ 0 & -\sin\varphi & \cos\varphi \\ 0 & \sin\varphi & \cos\varphi \end{pmatrix}$$

$$\times \begin{pmatrix} 1 & 0 & 0 \\ 0 & \cos\phi_p & -\sin\phi_p \\ 0 & \sin\phi_p & \cos\phi_p \end{pmatrix} \begin{pmatrix} \cos\phi_r & 0 & \sin\phi_r \\ 0 & 1 & 0 \\ -\sin\phi_r & 0 & \cos\phi_r \end{pmatrix} \begin{pmatrix} \cos\phi_h & \sin\phi_h & 0 \\ -\sin\phi_h & \cos\phi_h & 0 \\ 0 & 0 & 1 \end{pmatrix}, \tag{A 1}$$

where φ is the angle of the beams relative to the vertical. The first and second right-hand-side matrices accounts for the transformation from radial velocity components to velocity in Cartesian coordinates system for the master and slave ADCP respectively. The third, fourth and fifth right-hand-side matrices accounts for the rotation to match with the Cartesian coordinates system of the master ADCP. ϕ_p, ϕ_r and ϕ_h are the pitch, roll and heading respectively of the slave ADCP relative to the master ADCP.

References

1. Lazure P, Dumas F. 2008 An external-internal mode coupling for a 3D hydrodynamical model for applications at regional scale (MARS). *Adv. Water Resour.* **31**, 233–250. (doi:10.1016/j.advwatres.2007.06.010)
2. Bailly du Bois P, Dumas F, Solier L, Voiseux C. 2012 In-situ database toolbox for short-term dispersion model validation in macro-tidal seas, application for 2D-model. *Cont. Shelf Res.* **36**, 63–82. (doi:10.1016/j.csr.2012.01.011)
3. Thiébot J, Bailly du Bois P, Guillou S. 2015 Numerical modeling of the effect of tidal stream turbines on the hydrodynamics and the sediment transport—Application to the Alderney Race (Raz Blanchard), France. *Renew. Energy* **75**, 356–365. (doi:10.1016/j.renene.2014.10.021)
4. Robins PE, Neill SP, Lewis MJ, Ward SL. 2015 Characterising the spatial and temporal variability of the tidal-stream energy resource over the northwest European shelf seas. *Appl. Energy* **147**, 510–522. (doi:10.1016/j.apenergy.2015.03.045)
5. Guillou N, Chapalain G. 2017 Assessing the impact of tidal stream energy extraction on the Lagrangian circulation. *Appl. Energy* **203**, 321–332. (doi:10.1016/j.apenergy.2017.06.022)
6. Neill SP, Vögler A, Goward-Brown AJ, Baston S, Lewis MJ, Gillibrand PA, Waldman S, Woolf DK. 2017 The wave and tidal resource of Scotland. *Renew. Energy* **114**, 3–17. (doi:10.1016/j.renene.2017.03.027)
7. Thiébot J, Guillou N, Guillou S, Good A, Lewis M. 2020 Wake field study of tidal turbines under realistic flow conditions. *Renew. Energy* **151**, 1196–1208.
8. Lu Y, Lueck RG. 1999 Using a broadband ADCP in a tidal channel. Part II: turbulence. *J. Atmos. Ocean. Technol.* **16**, 1568–1579. (doi:10.1175/1520-0426(1999)016<1568:UABAIA>2.0.CO;2)
9. Rippeth TP, Williams E, Simpson JH. 2002 Reynolds stress and turbulent energy production in a tidal channel. *J. Phys. Oceanogr.* **32**, 1242–1251. (doi:10.1175/1520-0485(2002)032<1242:RSATEP>2.0.CO;2)
10. Korotenko K, Sentchev A, Schmitt FG, Jouanneau N. 2013 Variability of turbulent quantities in the tidal bottom boundary layer: case study in the eastern English Channel. *Cont. Shelf Res.* **58**, 21–31. (doi:10.1016/j.csr.2013.03.001)
11. McMillan JM, Hay AE, Lueck RG, Wolk F. 2016 Rates of dissipation of turbulent kinetic energy in a high Reynolds number tidal channel. *J. Atmos. Ocean. Technol.* **33**, 817–837. (doi:10.1175/JTECH-D-15-0167.1)
12. Guerra M, Thomson J. 2017 Turbulence measurements from five-beam acoustic Doppler current profilers. *J. Atmos. Ocean. Technol.* **34**, 1267–1284. (doi:10.1175/JTECH-D-16-0148.1)
13. Lueck RG, Wolk F, Yamazaki H. 2002 Oceanic velocity microstructure measurements in the 20th century. *J. Oceanogr.* **58**, 153–174. (doi:10.1023/A:1015837020019)
14. Thomson J, Polagye B, Richmond M, Durgesh V. 2010 Quantifying turbulence for tidal power applications. In *OCEANS 2010*, pp. 1–8. Seattle, WA: IEEE.
15. Thomson J, Polagye B, Durgesh V, Richmond MC. 2012 Measurements of turbulence at two tidal energy sites in Puget Sound, WA. *IEEE J. Ocean. Eng.* **37**, 363–374. (doi:10.1109/JOE.2012.2191656)
16. McCaffrey K, Fox-Kemper B, Hamlington PE, Thomson J. 2015 Characterization of turbulence anisotropy, coherence, and intermittency at a prospective tidal energy site: observational data analysis. *Renew. Energy* **76**, 441–453. (doi:10.1016/j.renene.2014.11.063)

17. Milne IA, Sharma RN, Flay RGJ, Bickerton S. 2013 Characteristics of the turbulence in the flow at a tidal stream power site. *Phil. Trans. R. Soc. A* **371**, 20120196. (doi:10.1098/rsta.2012.0196)
18. Sentchev A, Thiébaut M, Schmitt FG. 2019 Impact of turbulence on power production by a free-stream tidal turbine in real sea conditions. *Renew. Energy* **147**, 1932–1940. (doi:10.1016/j.renene.2019.09.136)
19. Thomson J, Kilcher L, Richmond M, Talbert J, DeKlerk A, Polagye B, Guerra M, Cienfuegos R. 2013 Tidal turbulence spectra from a compliant mooring. In *1st Marine Energy Technology Symposium, Washington, DC, 10–11 April*. METS2013.
20. Thiébaut M, Filipot J-F, Maisondieu C, Damblans G, Duarte R, Droniou E, Chaplain N, Guillou S. 2019 A comprehensive assessment of turbulence at a tidal-stream energy site influenced by wind-generated ocean waves. *Energy* **191**, 116550. (doi:10.1016/j.energy.2019.116550)
21. Lohrmann A, Hackett B, Røed LP. 1990 High resolution measurements of turbulence, velocity and stress using a pulse-to-pulse coherent sonar. *J. Atmos. Ocean. Technol.* **7**, 19–37. (doi:10.1175/1520-0426(1990)007<0019:HRMOTV>2.0.CO;2)
22. Lu Y, Lueck RG. 1999 Using a broadband ADCP in a tidal channel. Part I: mean flow and shear. *J. Atmos. Ocean. Technol.* **16**, 1556–1567. (doi:10.1175/1520-0426(1999)016<1556:UABAIA>2.0.CO;2)
23. Stacey MT, Monismith SG, Burau JR. 1999 Measurements of Reynolds stress profiles in unstratified tidal flow. *J. Geophys. Res.* **104**, 10935–10949. (doi:10.1029/1998JC900095)
24. Whipple AC, Luettich RA, Seim HE. 2006 Measurements of Reynolds stress in a wind-driven lagoonal estuary. *Ocean Dyn.* **56**, 169–185. (doi:10.1007/s10236-005-0038-x)
25. Wiles PJ, Rippeth TP, Simpson JH, Hendricks PJ. 2006 A novel technique for measuring the rate of turbulent dissipation in the marine environment. *Geophys. Res. Lett.* **33**. (doi:10.1029/2006GL027050)
26. Vermeulen B, Hoitink AJF, Sassi MG. 2011 Coupled ADCPs can yield complete Reynolds stress tensor profiles in geophysical surface flows. *Geophys. Res. Lett.* **38**. (doi:10.1029/2011GL046684)
27. Pieterse A, Filipot J-F, Maisondieu C, Kilcher L, Chaplain N. 2017 Coupled ADCP measurements for tidal turbulence characterization. In *Proceedings of the 12th European Wave and Tidal Energy Conference, Cork, Ireland*, pp. 1–8.
28. Shaw WJ, Trowbridge JH. 2001 The direct estimation of near-bottom turbulent fluxes in the presence of energetic wave motions. *J. Atmos. Ocean. Technol.* **18**, 1540–1557. (doi:10.1175/1520-0426(2001)018<1540:TDEONB>2.0.CO;2)
29. Feddersen F, Williams III AJ. 2007 Direct estimation of the Reynolds stress vertical structure in the nearshore. *J. Atmos. Ocean. Technol.* **24**, 102–116. (doi:10.1175/JTECH1953.1)
30. Rosman JH, Hench JL, Koseff JR, Monismith SG. 2008 Extracting Reynolds stresses from acoustic Doppler current profiler measurements in wave-dominated environments. *J. Atmos. Ocean. Technol.* **25**, 286–306. (doi:10.1175/2007JTECHO525.1)
31. Filipot J-F, Prevosto M, Maisondieu C, Le Boulluec M, Thomson J. 2015 Wave and turbulence measurements at a tidal energy site. In *Proceedings of a meeting held 2–6 March 2015, St. Petersburg, FL*, pp. 198–206. IEEE Catalog Number:CFP15CWT-POD.
32. Ardhuin F. 2012 Prévisions de vagues (WW3) pour la façade Golfe de Gascogne / Nord Atlantique (grille non structurée) (WW3-NORGAS-UG).
33. Durgesh V, Thomson J, Richmond MC, Polagye BL. 2014 Noise correction of turbulent spectra obtained from acoustic Doppler velocimeters. *Flow Meas. Instrum.* **37**, 29–41. (doi:10.1016/j.flowmeasinst.2014.03.001)
34. McMillan JM, Hay AE. 2017 Spectral and structure function estimates of turbulence dissipation rates in a high-flow tidal channel using broadband ADCPs. *J. Atmos. Ocean. Technol.* **34**, 5–20. (doi:10.1175/JTECH-D-16-0131.1)
35. Williams E, Simpson JH. 2004 Uncertainties in estimates of Reynolds stress and TKE production rate using the ADCP variance method. *J. Atmos. Ocean. Technol.* **21**, 347–357. (doi:10.1175/1520-0426(2004)021<0347:UIEORS>2.0.CO;2)
36. Frish U. 1995 *The legacy of A.N. Kolmogorov*. Cambridge, UK: Cambridge University Press.
37. Pope SB. 2000 *Turbulent flows*. Cambridge, UK: Cambridge University Press.

38. Rippeth TP, Simpson JH, Williams E, Inall ME. 2003 Measurement of the rates of production and dissipation of turbulent kinetic energy in an energetic tidal flow: Red Wharf Bay revisited. *J. Phys. Oceanogr.* **33**, 1889–1901. (doi:10.1175/1520-0485(2003)033<1889:MOTROP>2.0.CO;2)
39. Osalusi E, Side J, Harris R. 2009 Reynolds stress and turbulence estimates in bottom boundary layer of Fall of Warness. *Int. Commun. Heat Mass Transf.* **36**, 412–421. (doi:10.1016/j.icheatmasstransfer.2009.02.004)
40. Dewey R, Stringer S. 2007 Reynolds stresses and turbulent kinetic energy estimates from various ADCP beam configurations: theory. *J. Phys. Oceanogr.* 1–35.